Contents lists available at ScienceDirect

Ceramics International

journal homepage: www.elsevier.com/locate/ceramint

Rapid preparation of ZrC-SiC anti-ablation coating by joule-heating method

Xiangyu Ma [1], Kun Chen [*,1], Haibo Liu, Weining Li, Shaotian Qi, Ankang Jia, Zhaohe Jiang, Wei Xia, Dong Liu

State Key Laboratory of Heavy Oil Processing, College of Chemical Engineering, China University of Petroleum (East China), 66 Changjiang West Road, Huangdao District, Qingdao, Shandong, 266580, China

ARTICLE INFO

Keywords:
Coating
Joule heat
Anti-ablation
Silicate

ABSTRACT

In order to rapidly prepare self-healing coatings and significantly enhance the anti-ablation properties, the rapid sintering process of the coatings was achieved by the Joule heating method. Consequently, a structurally dense ZrC-SiC coating was successfully prepared on the surface of the graphite substrate within 60 s. The impact of ZrC content on the properties of ZrC-SiC coating was analyzed, and anti-ablation tests were conducted at 1500 °C. Through a series of experimental verifications, it was discovered that when the ratio of ZrC to SiC was 6:4, the anti-ablation efficiency of the coating reached the highest level, remaining stable at 97.61 %. Under this ratio, both the inert factor and the structural factor of the coating exhibited the lowest values. Meanwhile, the number of micropores and cracks on the coating surface also reached the minimum. Under the protection of the 60%ZrC-40%SiC coating, its average oxygen permeability was merely 0.12 %, and the carbon loss rate was as low as 0.13×10^{-6} g·cm^{-2} s^{-1}. In addition, this coating also demonstrated a relatively low porosity and a relatively high density.

1. Introduction

With the continuous advancement of aerospace technology, the demand for materials that can exist stably in extreme environments has become increasingly urgent, especially those materials capable of maintaining stable performance under the impact of high-temperature gas streams. Carbon materials have attracted considerable attention due to their favorable physical and chemical properties, such as high hardness, high strength, excellent thermal conductivity, corrosion resistance and chemical stability, along with their melting point as high as 3580 °C [1–3]. Nevertheless, despite the extremely high melting point of carbon materials, they begin to be affected by oxidation when the temperature reaches 500–600 °C [4]. Therefore, in order to address the issue of carbon materials being prone to oxidation under high-temperature conditions, antioxidant coatings are prepared on the surface of carbon materials to enhance their resistance to high-temperature oxidation [5,6].

To date, the technologies for coating preparation encompass chemical vapor deposition (CVD), physical vapor deposition (PVD), sol-gel process, solution impregnation and pack cementation [7]. Nevertheless, each of these techniques is associated with certain limitations. Specifically, the CVD method suffers from environmental and safety concerns, which deposition rate is relatively low [8]. The PVD method demands a prolonged duration for coating fabrication, and the resultant coatings exhibit inferior performance in terms of uniformity, hardness and impact resistance [9]. The sol-gel process not only entails a lengthy preparation period but also involves the utilization of organic solvents with potential hazards, in addition to the high cost of metal alkoxide raw materials [10]. The solution impregnation method encounters difficulties in precisely controlling the thickness and uniformity of the coatings [11]. The pack cementation method consumes a significant amount of energy due to the requisite long-duration sintering, which consequently affects its application efficiency [12]. In the context of the requirements for anti-ablation coatings in high-temperature environments, compactness constitutes a pivotal aspect of coating performance. However, the traditional sintering densification process for coatings typically extends over several hours, which not only leads to low production efficiency but also incurs substantial energy consumption. Zhu et al. [13]. spent 3.5 h preparing $TaSi_2$-WSi_2 and ZrB_2-$MoSi_2$-$ZrSi_2$ composite coatings on the Ta10W alloy surface by the slurry sintering method. Yan et al. [14]. spent 18 h preparing PDCs coatings on the SiBCN ceramic substrate through the pre-brushing and sintering

---

[*] Corresponding author.
E-mail address: chenkun@upc.edu.cn (K. Chen).
[1] These authors contributed to the work equally and should be regarded as co-first authors.

https://doi.org/10.1016/j.ceramint.2025.01.555
Received 20 November 2024; Received in revised form 12 January 2025; Accepted 29 January 2025

Please cite this article as: Xiangyu Ma et al., *Ceramics International,* https://doi.org/10.1016/j.ceramint.2025.01.555

method. By comparison, joule heating sintering significantly shortens the sintering time of coatings, which can not only improve the efficiency of coating preparation but also reduce energy consumption to a great extent. Meanwhile, rapid sintering can prevent the growth of grain size and maintain the original excellent properties of the substance [15]. To obtain high-quality coatings with enhanced efficiency, we innovatively employ the Joule heat sintering approach. This method enables rapid densification of the coating within a mere 60 s through rapid temperature elevation, and its sintering efficiency considerably surpasses that of conventional heating furnaces.

As an outstanding coating material, ZrC has a melting point as high as 3540 °C, a Mohs hardness as high as 8–9, and a thermal conductivity reaching 20–30 W/(m·K). Consequently, ZrC has been extensively employed within the coating material regime [16]. Ma et al. [17] fabricated ZrB_2-SiC-ZrC coatings via plasma spraying technology. The experimental results demonstrated that these coatings manifested excellent anti-ablation. Ding et al. [18] synthesized ZrC nano-ceramic coatings using double glow discharge sputtering technology. The ensuing experimental verifications attested to the coatings' good bonding strength and mechanical properties. Liu et al. [19] prepared ZrC-$MoSi_2$ and ZrC-SiC composite coatings by means of vacuum plasma spraying. The experimental investigations uncovered that these composite coatings possessed excellent anti-ablation. Da et al. [20] prepared CrMnFeCoNi composite coatings reinforced by refractory carbides (NbC and ZrC) through laser cladding technology and probed into their wear and antioxidant properties. The experimental outcomes signified that the CrMnFeCoNi composite coatings reinforced by (NbC and ZrC) exhibited excellent anti-ablation and wear resistance. In summary, ZrC coatings are endowed with favorable physical properties and outstanding anti-ablation performance, rendering them highly valuable in various relevant applications and research fields.

Recently, silicate glass layers, owing to their favorable anti-ablation capabilities, have been frequently employed as materials in coating systems. Silicon-containing materials are often incorporated into such coating systems. Consequently, during the oxidation process, a silicate glass layer can be formed, which subsequently enhances the anti-ablation of the coating. Additionally, silicates possess self-healing properties and are capable of self-healing cracks that emerge in the coating during the ablation process [21–23]. Takumi et al. [24] added SiC into the $Yb_2Si_2O_7$ coating to enhance the self-healing property of the coating. The results of the crack healing experiment manifested that the generated silicate exhibited crack self-healing characteristics. Fan et al. [25] utilized the sol-gel method to form borosilicate glass by adding SiC and boron-based precursors. A dense and uniform borosilicate glass coating was formed during the oxidation process. The experimental results demonstrated that the coating exhibited good thermal shock resistance, seawater corrosion resistance, and excellent self-healing capabilities. Zhou et al. [26] conducted an investigation into the oxidation and self-heal processes of SiC from the perspectives of thermodynamics and kinetics. The experimental results indicated that as the temperature rises, pores were generated on the surface of the coating due to the change in temperature. Oxygen would diffuse along these pores, and then the oxygen reacted with SiC to form self-healing SiO_2. Moreover, the mechanical properties of the coating were further improved as the temperature increases. Ou et al. [27] prepared ZrB_2-SiO_2 coatings on the surface of SiC-coated C/C composites. $ZrSiO_4$, B_2O_3, SiO_2 and ZrO_2 were formed during the heating process. The experimental results signified that the formation of $ZrSiO_4$ inhibited crack formation and augmented the antioxidant performance of the coating. In conclusion, the silicate generated during the heating process can repair cracks produced at high temperatures, further preventing the corrosion of the substrate by oxygen and thus improving the anti-ablation of the coating. Therefore, SiC modified ZrC coatings have significant potential application value.

In this study, the ZrC-SiC coating was prepared on the surface of the graphite by utilizing the Joule heating method. A dense coating could be fabricated on the graphite surface within 60 s. A dense coating was formed on the graphite surface within 60 s. To conduct a more comprehensive analysis of the properties of the coating, a system composed of standard samples, substrate samples, and coating samples was established for evaluation. Through experimental verification, it was found that the anti-ablation efficiency of 60%ZrC-20%SiC reached the highest level, stably maintaining at 97.61 %. Under this proportion, both the inert factor and the structural factor of the coating exhibited the lowest values. Meanwhile, the number of micropores and cracks on the coating surface also reached the minimum, with its average oxygen permeability being only 0.12 % and the carbon loss rate as low as 0.13×10^{-6} $g \cdot cm^{-2}$ s^{-1}. In addition, this coating also demonstrated a relatively low porosity and a relatively high density.

2. Experimental procedure

2.1. Materials and coatings preparation

The materials used in this experiment are SiC (purity>99.9 %, median particle size 40 nm), ZrC (purity>99.9 %, median particle size 2–5 μm), SiO_2 (purity>99.9 %, median particle size 20 μm), and graphite plate (purity 98 %), all from Shanghai McLean Biochemical Technology Co. LTD.

The coating materials were prepared by the Joule heating method under vacuum conditions, and the preparation process is illustrated in Fig. 1. Firstly, graphite sheets with a diameter of 10 mm and a thickness of 1 mm were polished and used as substrates to prepare coating samples. The materials of 80%ZrC-20%SiC (8 ZS), 60%ZrC-40%SiC (6 ZS), 40%ZrC-60%SiC (4 ZS), and 20%ZrC-80%SiC (2 ZS) were ball-milled at a rotational speed of 500 rpm for 1 h, respectively. Mix the SiO_2 powder with the sodium silicate solution. In order to uniformly control the thickness of the transition layer, use a spatula to take 0.1 g of the mixture and evenly coat it on the surface of the graphite sheet, aiming to improve the difference in thermal expansion coefficients between the graphite substrate and the coating. Subsequently, utilize a hydraulic press to press the mixed coating powder onto the substrate surface at 10 MPa for 10 min. To control the thickness of the coating, place 0.5 g and 0.3 g of samples above and below the graphite substrate respectively. The sintering process is carried out by a Joule heating device (FJH-2024A, SAIYIN NEW MATERIALS, China). Based on the properties of SiC and ZrC and after multiple sintering tests, a dense and complete coating material can be obtained when the sintering program is set as follows: 700 °C-10 s, 1000 °C-10 s, 1500 °C-10 s, and 2000 °C-30 s. The process of Joule heat sintering can be seen in Fig. S1. To verify the ablation status of the graphite substrate under the protection of the coating, standard samples of pure coating were also prepared simultaneously for comparison.

2.2. Ablation testing and characterization

The coating samples and the standard samples were subjected to ablation tests at a temperature of 1500 °C in air. The fuel gas employed for the tests was petroleum gas. The heat flux of the fuel gas was adjusted to 1.8 MW/m^2. The temperature was controlled within the range of 1500 ± 50 °C by means of an infrared thermometer. The details of the ablation tests can be seen in Fig. S2. Before conducting the ablation tests, it was required to place the coating samples and the standard samples in an oven and dry them at 70 °C for 24 h. The dried samples were then subjected to an ablation test for 180 min. We weighed the samples at intervals of 5 min within the 0–10 min range, at intervals of 10 min from 10 to 40 min, at intervals of 20 min from 40 to 120 min, and at intervals of 30 min from 120 to 180 min. The weight changes of the samples were analyzed using Eq. (1) [28].

$$G\% = \sum_{j=1}^{n} \frac{\left(m_j - m_{j-1}\right)}{m_0} \qquad (1)$$

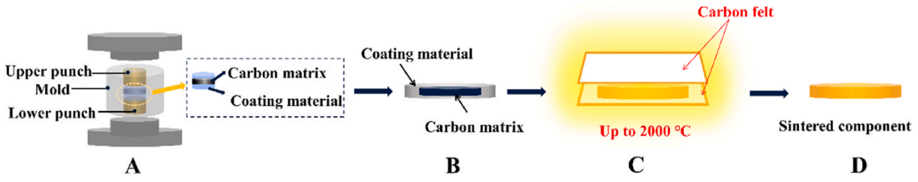

Fig. 1. Illustration of the process flow for the preparation of ZrC-SiC coatings by the Joule-heating method, A Coating pressing; B Coating sample; C Joule-heating sintering; D Sintered sample.

m_{j-1} (g) denotes the weight of the sample at time j-1(min); m_j (g) denotes the weight of the sample at time j (min); m_0 (g) denotes the weight of the sample before ablation.

The phase composition of the ZrC-SiC coatings was determined by X-ray diffraction (XRD, Bruker D8 ADVANCE, BRUKER AXS, Germany) using a Cu K(α) at a current of 30 mA and a voltage of 40 KV, and the organisational structure of the coatings was determined by scanning electron microscopy (SEM, FEI QUANTA FEG 250, Thermo Fisher America). In addition, the chemical state of the samples was analyzed by X-ray photoelectron spectroscopy (XPS, ESCALAB Xi+, Thermo Fisher, America).

3. Results analysis and discussion

3.1. Microstructure of Joule-heated sintered ZrC-SiC coatings

In order to investigate the surface morphology of the coating after sintering, Fig. 2 presents the Backscattering SEM (BSE) images of the ZrC-SiC coating prior to ablation. As can be seen from the figure, in the unsintered Fig. 2(a), a relatively large number of cracks and pores are observable, whereas in the sintered Fig. 2(b–e), there are fewer cracks and pores. It can thus be inferred that the coating after Joule heat sintering exhibits a relatively high compactness on its surface, with no obvious cracks, demonstrating favorable microstructural characteristics.

Fig. 3 presents the cross-sectional backscattered images of the coating samples after Joule heat sintering. In this study, the carbon matrix was selected as discs with a thickness of 1 mm and a diameter of 15 mm. For the 8 ZS-2 ZS, the thicknesses of the SiO_2 layers were 0.68 mm, 0.45 mm, 0.44 mm and 0.39 mm respectively, while the thicknesses of the ZrC-SiC layers were 1.07 mm, 1.22 mm, 1.00 mm and 1.90 mm respectively. The resin layer was introduced as a result of the mounting and polishing treatment performed on the samples to facilitate the observation of the cross-sectional morphology. As can be seen from Fig. 3, the bonding between the coating and the carbon substrate is in a favorable condition, and no obvious cracks are observed on their cross-sections. Moreover, due to the existence of the SiO_2 transition layer, no significant deformation occurs between the ZrC-SiC coating and the carbon substrate. It can be concluded from the magnified Fig. 3(e–h) that the ZrC-SiC coating exhibits a uniform and dense state after undergoing Joule heat sintering.

3.2. 1500 °C anti-ablation mechanism analysis

In order to investigate the compositional changes of the ZrC-SiC coating after ablation in air at 1500 °C, the XRD results on the surface of the ZrC-SiC coating are presented in Fig. 4. The resin layer was subjected to mounting and polishing treatment for the purpose of observing the cross-sectional morphology of the coated samples. When analyzing the XRD and XPS of the surfaces of the coated samples, the surfaces did not contain the resin layer. According to the oxidation reactions (2)–(4) [27], after 180 min of ablation, SiO_2, ZrO_2, and $ZrSiO_4$ phases were generated on the surface of the coating [29–34]. It can be observed from Fig. 4 that as the content of ZrC decreases, the peaks of ZrC in the samples become significantly smaller, and meanwhile the peaks of SiC in 2 ZS also decrease. This is because when the content of ZrC is relatively low, it is impossible to generate self-healing $ZrSiO_4$ on the surface of the

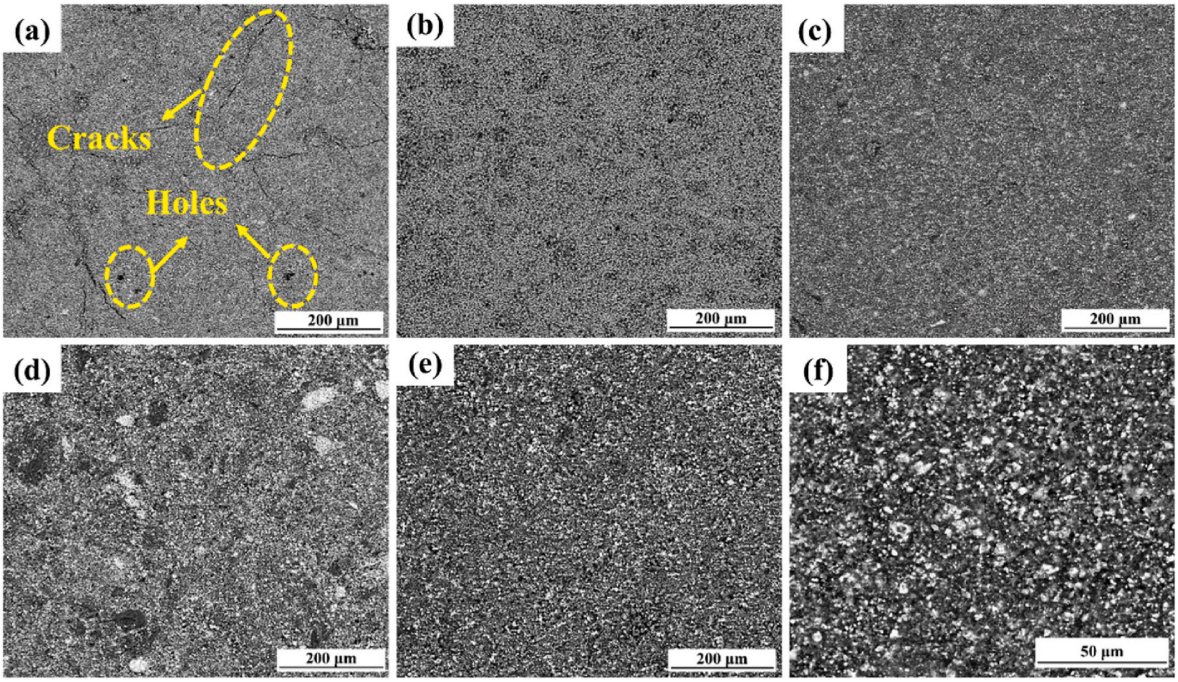

Fig. 2. BSE images of the surface of ZrC-SiC coatings with different contents: (a) before sintering; (b) 8 ZS; (c) 6 ZS; (d) 4 ZS; (e) 2 ZS; (f) enlargement of 6 ZS.

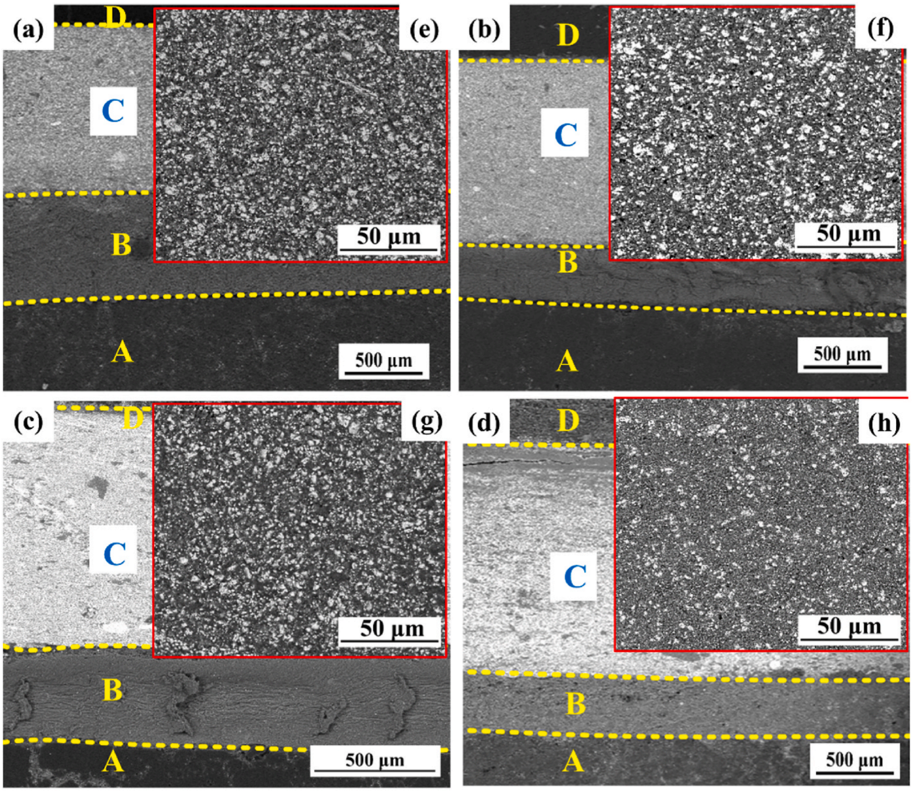

Fig. 3. Cross-sectional BSE images of the coated samples before ablation, (a) 8 ZS; (b) 6 ZS; (c) 4 ZS; (d) 2 ZS; (e–h) are magnified images of the C components of (a–d); A: carbon matrix; B: SiO_2 layer; C: ZrC-SiC layer; D: resin layer.

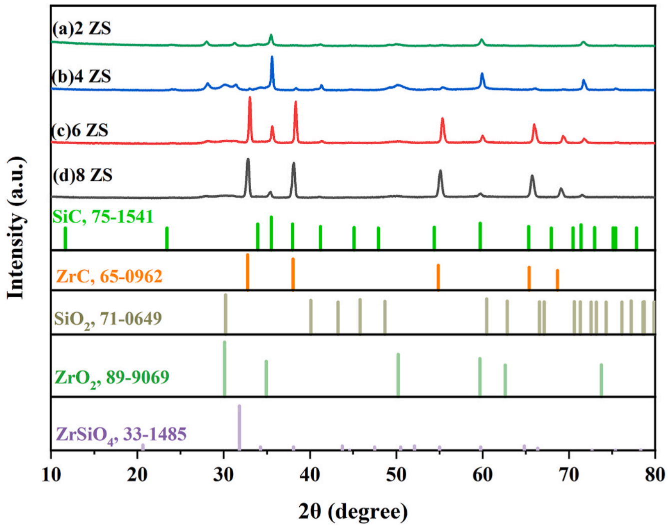

Fig. 4. XRD analysis of ZrC-SiC coated 1500 °C surface after ablation.

coating, which leads to the oxidative decomposition of the coating. As a result, SiC is oxidized into SiO_2, ultimately resulting in the decrease of the peaks of SiC in 2 ZS. Therefore, the formation of multi-component oxides contributes to enhancing the antioxidant effect of the coating.

$$SiC(s)+2O_2(g)\rightarrow SiO_2(s)+CO_2(g) \quad (2)$$

$$ZrC(s)+2O_2(g)\rightarrow ZrO_2(s)+CO_2(g) \quad (3)$$

$$ZrO_2(s)+SiO_2(s)\rightarrow ZrSiO_4(s) \quad (4)$$

In order to further investigate the chemical state of surface oxides of the coating after ablation at 1500 °C, XPS analysis was performed on the ablated coating samples. The results are shown in Fig. 5. The characteristic peaks of the Zr 3d, O 1s, and Si 2p spectra were fitted [35–37]. From the analysis of the figure, it can be seen that Si-O-Zr bonds were formed in O 1s and Si 2p, further indicating that $ZrSiO_4$ with self-healing properties was formed during the ablation process of the coating. In Fig. 5(a), the peak of Zr is relatively low, while in Fig. 5(d), the peak of SiC is relatively high. The reason for this phenomenon lies in the fact that XPS is a semi-quantitative analysis of the surface. During the high-temperature oxidation process, $ZrSiO_4$ with fluidity will be formed on the surface of the coating. This substance can permeate into the interior of the coating and then repair the pores inside the coating. Consequently, the peak of Zr on the surface of the coating is relatively low, while the peak of SiC is relatively high. It can be observed from Fig. 5(c–g, k, o) and (d, h, I, p) that the peak area of the Si-O-Zr bond undergoes significant changes. Among them, the peak areas of the Si-O-Zr bond in (g) and (h) are the largest, which indicates that the retention amount of silicon-zirconium oxides is higher for 6 ZS.

For the purpose of investigating the weight changes of the coating samples and the standard samples during the ablation process, the detailed analysis and weight changes are illustrated in Fig. S3. It can be seen therefrom that when the content of ZrC is 60 %, the coating structure is more compact, and the oxide film $ZrSiO_4$ formed on the coating surface can prevent further oxidative weight gain inside the coating. However, the weight gain rate of the standard samples is significantly higher than that of the coating samples. This is because the oxidation of the carbon substrate leads to weight loss. Consequently, the weight gain rates of the standard samples and the coating samples cannot accurately reflect the protective effect of the coating. In order to conduct a practical study of the protective effect of the coatings, the cumulative ablation resistance efficiency of the ZrC-SiC coatings was subsequently analyzed by means of Eq. (5) [28].

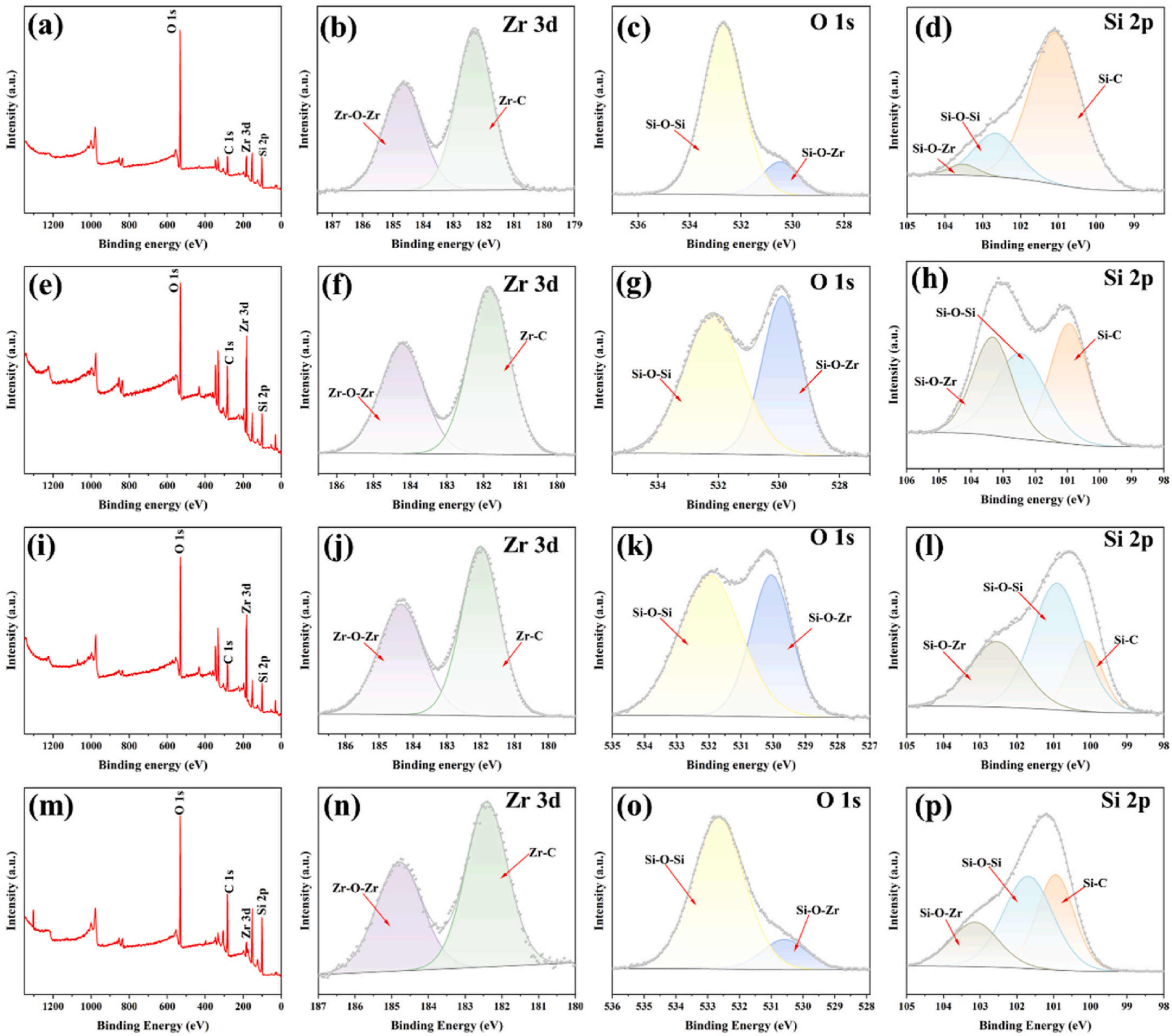

Fig. 5. XPS analysis of the coating surface after ablation at 1500 °C. (a–d) 8 ZS; (e–h) 6 ZS; (i–l) 4 ZS; (m–p) 2 ZS.

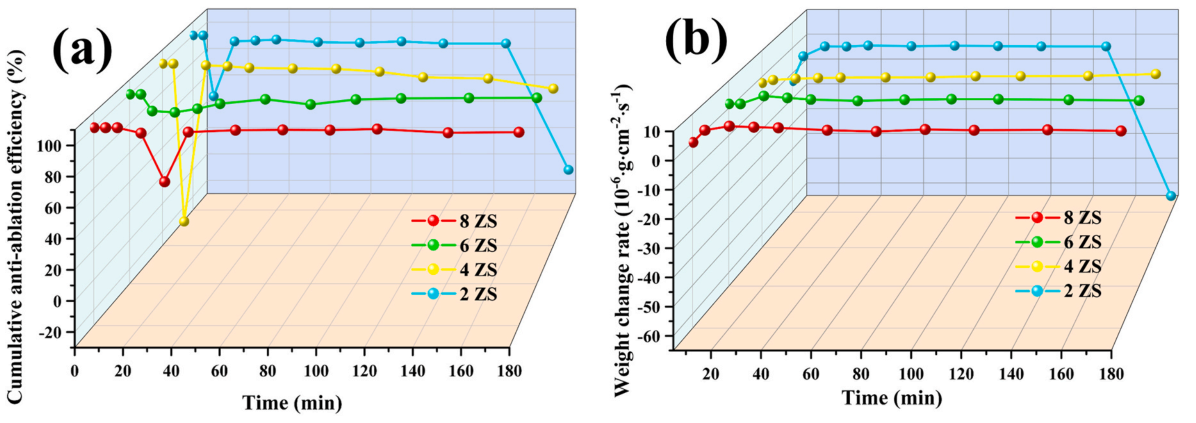

Fig. 6. (a) Cumulative anti-ablative efficiency of ZrC-SiC coating at 1500 °C ablation; (b) Rate of weight change curve of standard sample at 1500 °C.

$$\gamma_{k,j} = \left[1 - \frac{(m_{p,k,j} - m_{p,k,0}) - (m_{q,k,j} - m_{q,k,0})}{(m_{s,j} - m_{s,0})}\right] \tag{5}$$

$\gamma_{k,j}$ (%) is the cumulative anti-ablation efficiency; $m_{p,k,j}$ ($g \cdot cm^{-2}$) is the weight per unit area of the k-component standard sample at the j-moment (min); $m_{q,k,j}$ ($g \cdot cm^{-2}$) is the weight per unit area of the k-component coated sample at the j-moment (min); $m_{s,j}$ ($g \cdot cm^{-2}$) is the weight per unit area of the graphite substrate at the j-moment (min).

Fig. 6 shows the cumulative anti-ablation and rate of change of weight analysis of the coating. Fig. 6(a) presents the analysis of the cumulative anti-ablation efficiency of coatings with different compositions during the ablation process at 1500 °C. As can be seen from Fig. 6 (a), the anti-ablation efficiency of the coatings exhibits a trend of first decreasing, then increasing, and finally tending to stabilize. During the stage of decreasing anti-ablation efficiency, the coatings rely on their own structures to resist ablation, which is a dynamic anti-ablation process. During the stage of increasing anti-ablation efficiency, an oxide layer is formed within the coating, and the anti-ablation is mainly borne by this oxide layer. Therefore, these two stages can be respectively referred to as the dynamic stage and the inert stage of the coating. According to Fig. 6(a), as the content of ZrC gradually decreases, the cumulative anti-ablation efficiencies are 97.04 %, 97.61 %, 82.17 %, and 0 %, respectively. The reason why the cumulative anti-ablation efficiency of the 2 ZS is 0 % is that the coating peels off at 180 min. Therefore, when the addition amount of ZrC is 60 %, the coating exhibits the best anti-ablation performance. This is due to the inert effect of the zirconium silicate glass layer formed by the coating, which enables the coating to possess excellent anti-ablation performance and self-heal the defects generated during the ablation process in the inert stage.

$$V_k = \frac{1}{n}\sum_{j=1}^{n}\frac{(m_{p,k,j} - m_{p,k,j-1})}{t_j} \tag{6}$$

V_k (10^{-6} g cm^{-2} s^{-1}) is the rate of weight change of the standard sample; $m_{p,k,j}$ ($g \cdot cm^{-2}$) is the weight per unit area of component k at the jth moment of the standard sample; t_j (s) is the time interval.

To more accurately explore the properties of ZrC-SiC coatings with different proportions, it is necessary to eliminate the influence of the carbon substrate. The anti-ablation mechanism of the coating is analyzed by studying the weight change rate of the standard samples, and the weight change rate is calculated according to Eq. (6) [28]. The results are shown in Fig. 6(b). When 20%ZrC is added, the weight change rate of the standard samples shows a significant increase. Moreover, when the addition amounts of ZrC are 40 % and 20 %, the weight change rates of the standard samples tend to be less than zero. This is due to the fact that as the content of Zr decreases, the content of generated ZrO_2 reduces, which leads to the decline in the yield of $ZrSiO_4$ with self-healing characteristics. When the content of $ZrSiO_4$ decreases, it becomes difficult to heal the defects generated in the coating during the ablation process [27]. The increase in the number of pores will lead to a greater penetration of oxygen in the coating, resulting in a relatively large change in the weight change rate. Based on the analysis of Fig. 6 (b), the weight change rate of the coating with an addition amount of 60%ZrC is more stable. The reason is that this coating forms a dense oxide layer during the ablation process and has good self-healing properties.

$$V_p = \frac{1}{n}\left[\sum_{j=1}^{n}\frac{(m_{p,k,j} - m_{p,k,j-1}) - (m_{q,k,j} - m_{q,k,j-1})}{t_j}\right] \tag{7}$$

$$W_k = \frac{1}{n}\sum_{j=1}^{n}\frac{V_k - V_s}{V_p} \times 100\% \tag{8}$$

V_p (10^{-6} g cm^{-2} s^{-1}) is the rate of loss of carbon; $m_{p,k,j}$ (g) is the weight per unit area of the standard sample; $m_{q,k,j}$ (g) is the weight per unit area of the coated sample; t_j (s) is the time interval; W_k (%) is the oxygen permeability; and V_s (10^{-6} g cm^{-2} s^{-1}) is the rate of change in the weight of the coated sample.

During the ablation process of the coating samples, the carbon substrate will experience attrition. In order to conduct a more comprehensive analysis of the loss status of the carbon substrate under the protection of the coating, the loss rate of the carbon substrate is calculated by means of Eq. (7) [28]. The results shown in Fig. 7 were obtained by taking the average value through five repeated experiments. The carbon loss rate of the obtained carbon substrate and the average anti-ablation efficiency are shown in Fig. 7(a). As the content of ZrC decreases from 80 % to 20 %, the carbon loss rates are successively 1.2 $\times 10^{-6}$, 0.13 $\times 10^{-6}$, 2.5 $\times 10^{-6}$ and 3.1 $\times 10^{-6}$ $g \cdot cm^{-2}$ s^{-1}, which indicates that the carbon loss rate of the 6 ZS is the lowest, and its average anti-ablation efficiency is the highest, reaching up to 96 %. The reason for the mass loss of the carbon substrate lies in the fact that oxygen permeates through the coating to come into contact with the carbon substrate, thereby causing the mass of the carbon substrate to decrease. Consequently, the oxygen permeability W_k of the coating is calculated by means of Eq. (8) [28], and the results are shown in Fig. 7(b). As the content of ZrC decreases from 80 % to 20 %, due to the fact that the zirconium silicate generated during the ablation process of the coating has a certain air-isolating effect and can repair the pores of the coating, the oxygen permeabilities of the coating are respectively 0.29 %, 0.12 %, 0.52 % and 2.3 %. Ou et al. [27] verified through the research on $ZrSiO_4$ that $ZrSiO_4$ can enhance the compactness of the coating and possess a certain function of isolating air. Meanwhile, $ZrSiO_4$ can heal the pores generated in the coating during the ablation process. The data show that the oxygen permeability of 6 ZS is the lowest, which means that it has good compactness, and correspondingly, its carbon loss rate is also the lowest.

During the ablation process, the protection of the coating exhibits dynamic characteristics, with its overall structure continuously changing along with the progress of ablation. To further evaluate the structural changes of the coating during the ablation process, the inert factor is employed to assess the oxygen-blocking performance of the oxides generated by the coating during the inert stage. Meanwhile, the structural factor is utilized to measure the oxygen-blocking performance of the coating's own structure during the ablation process. Consequently, the smaller the structural factor, the better the oxygen-blocking performance of the coating structure. The inert factor, on the other hand, conducts a quantitative analysis of the weight changes of the coating's oxide layer during the inert stage. Therefore, the smaller the inert factor, the better the oxygen-blocking performance of the oxide layer generated by the coating during the ablation process. The structural factor and inert factor of the coating were calculated according to Eqs. 9 and 10 [28].

$$\varepsilon_{s,k} = \frac{1}{n}\sum_{j=1}^{n}\frac{(m_{p,k,j} - m_{p,k,j-1}) - (m_{q,k,j} - m_{q,k,j-1})}{(m_{s,j-1} - m_{s,j})} \tag{9}$$

$$\varepsilon_{i,k} = \frac{1}{n}\sum_{j=1}^{n}\frac{(m_{p,k,j+2} - m_{p,k,j+1})}{t_j} \tag{10}$$

$\varepsilon_{s,k}$ (%) is the structural factor; $m_{p.k.j}$ ($g \cdot cm^{-2}$) is the mass per unit area of component k of the standard sample at moment j; $m_{q,k,j}$ ($g \cdot cm^{-2}$) is the mass per unit area of component k of the coating sample at moment j; t_j (s) is the time interval; and $\varepsilon_{i,k}$ (10^{-6} g cm^{-2} s^{-1}) is the inert factor.

As can be seen from Fig. 8, with the increase in the content of ZrC in the ZrC-SiC coating, the structural factors of the coating were 13.4 %, 9.7 %, 5.3 %, and 7.4 % successively. The data indicate that when 60% ZrC was added, a relatively low structural factor was obtained. This suggests that during the ablation process, the overall structure of the coating with 60%ZrC exhibits better oxygen-blocking performance and compactness, thereby being able to protect the carbon substrate more effectively. After the formation of the inert oxide layer of the coating, in

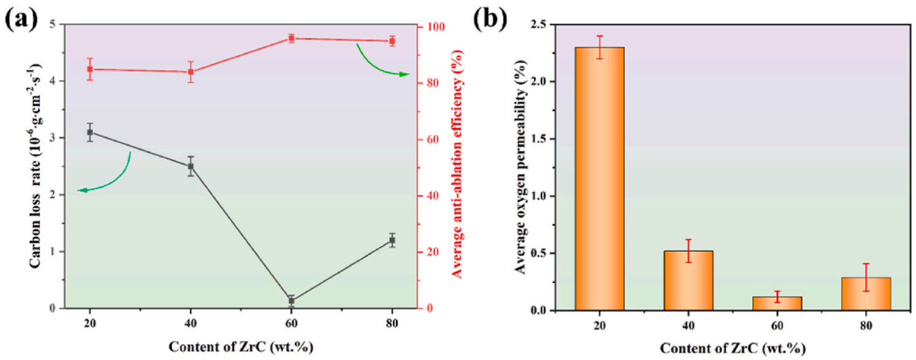

Fig. 7. (a) Carbon loss rate and average anti-ablation efficiency of coatings under ablation at 1500 °C; (b) Average oxygen permeability of coatings after ablation at 1500 °C.

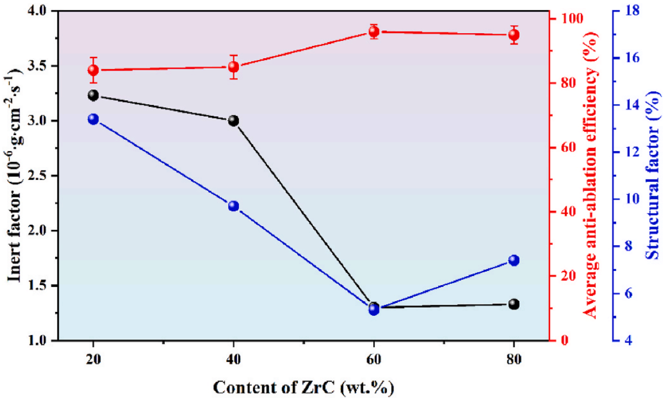

Fig. 8. Structural factor, inert factor and average ablative efficiency of ZrC-SiC coatings.

order to analyze the impact of this oxide layer on the coating properties, the inert factor was introduced for analysis. With the increase in the addition amount of ZrC, which can be obtained from the analysis of Fig. 8 that the inert factors were 3.23 × 10^{-6}, 3.01 × 10^{-6}, 1.30 × 10^{-6}, and 1.33 × 10^{-6} g·cm^{-2} s^{-1} respectively. The results show that 6 ZS has a relatively low inert factor. This implies that during the ablation process, the inert oxide layer generated by 6 ZS can enhance the compactness of the coating, repair the pores of the coating, improve the oxygen-blocking performance of the coating, and further prevent the further oxidation of the coating. Taking into account the structural factor, inert factor, and average anti-ablation efficiency of the coating, which can be concluded that 6 ZS possesses favorable structural and inert oxygen-blocking capabilities.

During the ablation process, cracks and pores were generated in the coating, and the formation of inert oxides healed the cracks and reduced the number of pores in the coating. The number of cracks and pores in the coating is one of the key factors affecting its compactness. To further investigate the changes in the compactness of ZrC-SiC coatings with different proportions during the ablation process, the Archimedes drainage method was employed to measure the changes in density, porosity, and compactness of the coating during the ablation process, thereby conducting an analysis of the compactness of the coating. The actual density, porosity, and compactness of the coating were calculated through Eqs 11–13 [38].

$$\rho_s = \frac{m_1}{m_3 - m_2}\rho_w \tag{11}$$

$$P = \frac{m_3 - m_1}{m_3 - m_2} \tag{12}$$

$$RD = \frac{\rho_s}{\rho_l} \tag{13}$$

ρ_s (g/cm^3) is the actual density of the material; P is the open porosity of the material; RD is the densification of the material; m_1 (g) is the weight of the material when it is completely dry; m_2 (g) is the weight of the material in deionized water; m_3 (g) is the weight of the material in air after it has fully absorbed water; ρ_w (g/cm^3) is the density of water; and ρ_l (g/cm^3) is the theoretical density of the material.

The theoretical density of the coating was calculated according to the law of mixtures for density, and the results are shown in Fig. 9. Fig. 9(a) represents the variation curve of the porosity of the coating under the ablation condition at 1500 °C. When the content of ZrC is within the range of 40%–80 %, the porosity of the coating shows a trend of first increasing and then decreasing. The reason is that in the initial stage of the ablation process, the coating relies on its own structure to play the role of anti-ablation. When air continuously permeates into the interior of the coating, the coating is constantly eroded by the air due to high temperature. As a result of the oxidation by the air, defects gradually emerge in the coating, which leads to an increase in the number of pores in the coating. Subsequently, under the action of high temperature, an inert oxide layer is generated in the coating. The appearance of this oxide layer played a repairing role for the pores generated in the coating in the initial stage, causing the porosity to decrease. Among them, the 6 ZS has a relatively low porosity. For the coating with 20%ZrC added, which porosity shows an increasing trend. The reason is that the 2 ZS has poor compactness, and the inert oxide layer is unable to repair the pores generated by high temperature. At 180 min, the coating completely peels off. Fig. 9(b) represents the compactness of the coating. When the addition amount of ZrC is within the range of 40%–80 %, the compactness shows a trend of first decreasing and then increasing, which indicates that when the pores in the coating expand under high temperature, its compactness will correspondingly decrease. And when the inert oxide layer appears and repairs the generated pores, the compactness will further increase. Among them, the 6 ZS has a relatively high density and excellent thermal shock resistance. The analysis of thermal shock resistance can be referred to Fig. S4. The compactness of 2 ZS shows a downward trend. The reason is that the structure of the coating is unable to withstand the impact of high-temperature ablation and fails to repair the defects generated during the ablation process of the coating, resulting in a continuous decrease in compactness.

In order to analyze the morphology of the coating after ablation, Fig. 10 presents the BSE analysis of the surface of the ZrC-SiC coating after ablation at 1500 °C. As shown in Fig. 10(b), there are no obvious holes and cracks on the surface. The reason lies in that 6 ZS exhibits excellent densification after sintering, and the inert oxide layer formed after ablation can self-heal the surface cracks and holes. However, a decrease in the ZrC content leads to a decrease in the structural stability of the coating, resulting in a decrease in its resistance to high

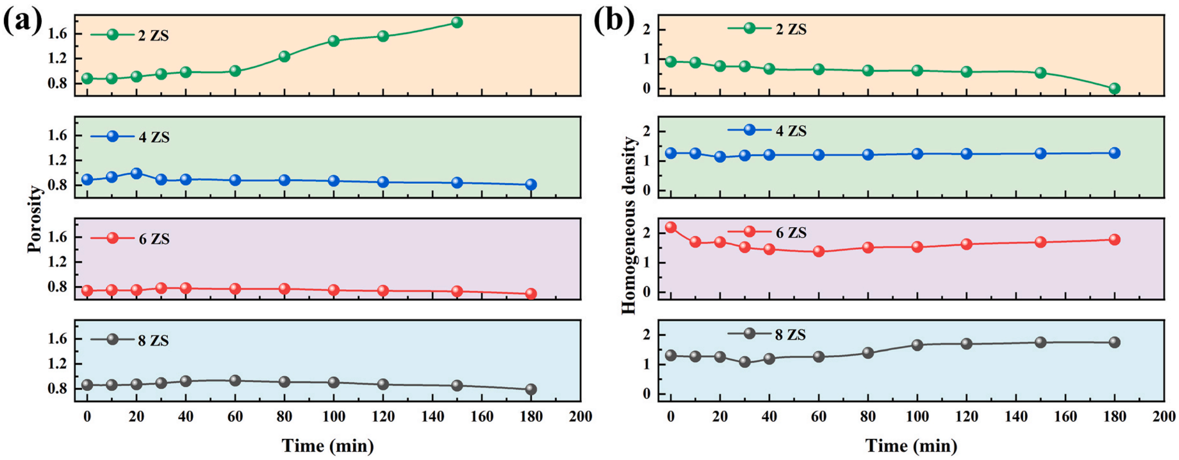

Fig. 9. Variation of (a) porosity (b) homogeneous density during ablation of ZrC-SiC coating 1500 °C.

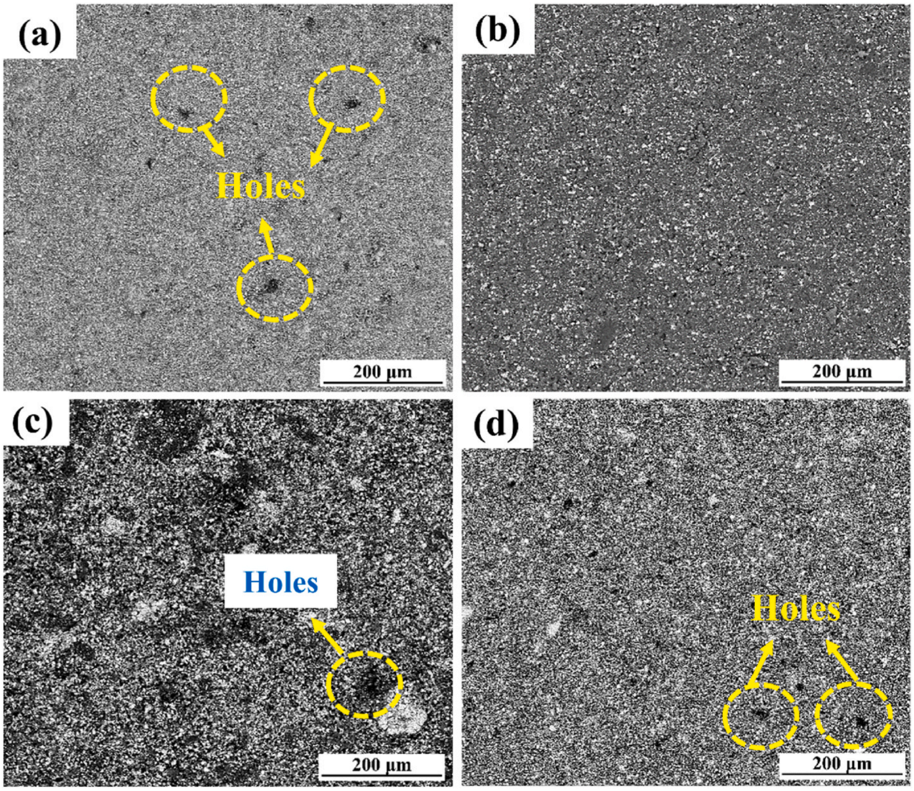

Fig. 10. BSE images of the ZrC-SiC coating surface after ablation at 1500 °C (a) 8 ZS; (b) 6 ZS; (c) 4 ZS; (d) 2 ZS.

temperatures and erosion, which ultimately leads to spalling of the coating during the ablation process. For 8 ZS, the surface after ablation is relatively dense, but it contains more holes. This is because although the structure of the 8 ZS is stable and can withstand the scouring of high-temperature gas streams, due to the insufficient content of SiC, it is unable to self-heal the cracks and holes on the coating surface. In conclusion, 6 ZS possesses a relatively good surface morphology and anti-ablation performance.

In order to research the cross-sectional morphology of the coating after ablation at 1500 °C, Fig. 11 shows the morphology and oxygen element distribution of the cross-section of the ablated coating samples. Fig. 11(a–c) are the cross-sectional BSE images of the coatings with 80%-40%ZrC after ablation at 1500 °C respectively. Among them, there are a few cracks and holes in the C layer of the 8 ZS, and relatively large cracks are present at the interface between the B and C layers of the 4 ZS. Fig. 11(d, e, f) are the distribution maps of oxygen elements in the cross-section. The cross-sections of the 8 ZS and 4 ZS contain a relatively large amount of oxygen elements, while the cross-section of the 6 ZS has the least amount of oxygen elements. This indicates that the coating with 60%ZrC added has a lower oxygen permeability, meaning that the 6 ZS possesses good densification and can more effectively prevent the infiltration of oxygen during the ablation process, thereby verifying the conclusion obtained previously, that is, the 6 ZS has a lower oxygen permeability. Fig. 11(g, h, i) are the magnified images at the coating interface. There are no obvious cracks at the interfaces of the 8 ZS and 4 ZS, with a few holes at the interface of the 8 ZS, and obvious cracks at the interface of the 4 ZS. The distribution of other elements is shown in Fig. S5. During the ablation process, under the erosion of high-

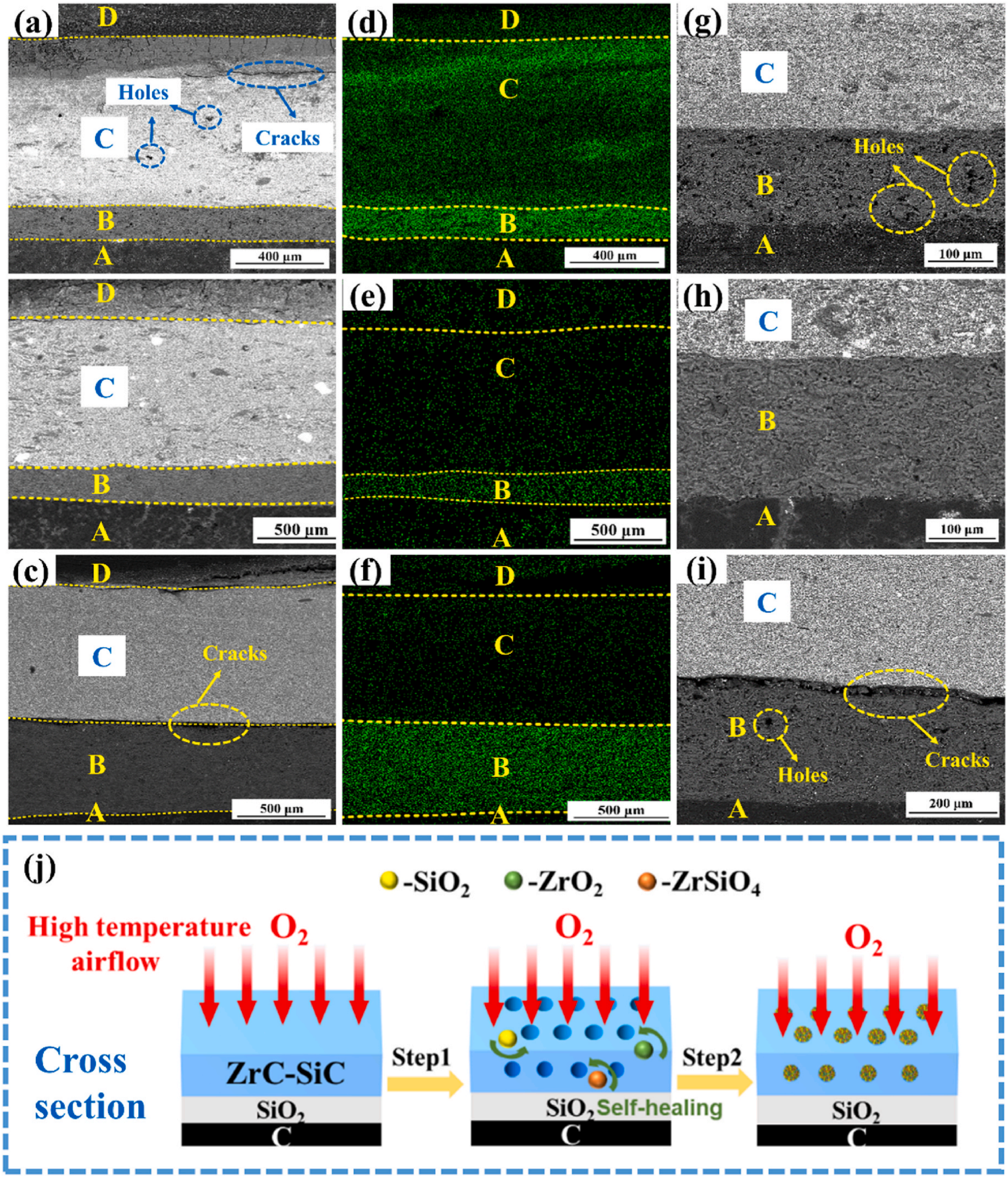

Fig. 11. Cross-sectional BSE (a–i) and self-healing process (j) of ZrC-SiC coatings after ablation at 1500 °C. (a) 8 ZS; (b) 6 ZS; (c) 4 ZS; (j) Self-healing process of ZrC-SiC coating; (d, e, f) Corresponding elemental oxygen analysis; (g, h, i) Enlarged views at the cross-section interface. A: carbon matrix; B: SiO_2 layer; C: ZrC-SiC layer; D: resin layer.

temperature gas streams, holes and cracks will be generated both inside and on the surface of the coating. The self-heal process of the coating is illustrated in Fig. 11(j). At this time, with the intrusion of oxygen, SiC and ZrC inside the coating react to form SiO_2, ZrO_2, and $ZrSiO_4$ oxide layers with self-healing characteristics. Eventually, the cracks and holes generated during the ablation process are repaired, thereby enhancing the densification of the coating.

4. Conclusions

In this work, the ZrC-SiC self-healing coating was rapidly prepared by means of Joule heating. A dense coating was fabricated on the graphite surface within 60 s and then ablated in air at 1500 °C for 180 min. Among them, the surface of the 60%ZrC-40%SiC coating after ablation had no obvious defects, and its cross-section also had no significant cracks and holes. Good compatibility was exhibited between the coating and the graphite substrate. The 60%ZrC-40%SiC coating prepared by the Joule heating method not only possessed an anti-ablation efficiency as high as 97.61 %, but also had a low oxygen permeability, a low carbon loss rate, a low porosity, and a high density. Moreover, its oxygen permeability was as low as 0.12 %, the carbon loss rate was as low as 0.13×10^{-6} g·cm^{-2} s^{-1}, the porosity was as low as 0.69, and the density reached 1.74. The coating materials fabricated by means of Joule heating have significantly reduced the consumption of energy to a large extent, making it a reality to prepare ceramic coating materials with high efficiency.

CRediT authorship contribution statement

Xiangyu Ma: Writing – original draft, Investigation, Data curation. **Kun Chen:** Investigation. **Haibo Liu:** Investigation. **Weining Li:** Investigation. **Shaotian Qi:** Investigation. **Ankang Jia:** Investigation. **Zhaohe Jiang:** Investigation. **Wei Xia:** Investigation. **Dong Liu:** Investigation.

Declaration of competing interest

The authors declare that they have no known competing financial interests or personal relationships that could have appeared to influence the work reported in this paper.

Appendix A. Supplementary data

Supplementary data to this article can be found online at https://doi.org/10.1016/j.ceramint.2025.01.555.

References

[1] M. Kim, Y. Kim, A thermo-mechanical properties evaluation of multi-directional carbon/carbon composite materials in aerospace applications, Aerospace 9 (2022) 461, https://doi.org/10.3390/aerospace9080461.

[2] J. Weerasinghe, K. Prasad, J. Mathew, et al., Carbon nanocomposites in aerospace technology: a way to protect low-orbit satellites, Nanomaterials 13 (2023) 1763, https://doi.org/10.3390/nano13111763.

[3] L. Kong, X. Zuo, S. Zhu, et al., Novel carbon-poly (silacetylene) composites as advanced thermal protection material in aerospace applications, Compos. Sci. Technol. 162 (2018) 163–169, https://doi.org/10.1016/j.compscitech.2018.04.038.

[4] J. V M Jr., J E S, K. T M, Dynamics of graphite oxidation at high temperature, J. Phys. Chem. C 122 (2018) 6602–6617, https://doi.org/10.1021/acs.jpcc.7b11772.

[5] C. Shi, Q. Xinchao, Z. Bowen, et al., Advances in antioxidation coating materials for carbon/carbon composites, J. Alloys Compd. 886 (2021) 161143, https://doi.org/10.1016/j.jallcom.2021.161143.

[6] Y. Li, F. Zeng, B. Gao, et al., Durable anti-oxidation mechanism and failure analysis of the $ZrSiO_4$ compound glass coating for carbon/carbon composite, Surf. Coating. Technol. 349 (2018) 233–241, https://doi.org/10.1016/j.surfcoat.2018.05.050.

[7] C. Yao, H. Lv, T. Zhu, et al., Effect of Mg content on microstructure and corrosion behavior of hot dipped Zn–Al–Mg coatings, J. Alloys Compd. 670 (2016) 239–248, https://doi.org/10.1016/j.jallcom.2016.02.026.

[8] G. Xiao, H. Zeng, S. Xu, et al., Preparation of Ti species coating hydrotalcite by chemical vapor deposition for photodegradation of azo dye, J. Environ. Sci. 60 (2017) 14–23, https://doi.org/10.1016/j.jes.2017.03.031.

[9] J. Xiao, Q. Guo, L. Wei, et al., Microstructures and phases of ytterbium silicate coatings prepared by plasma spray-physical vapor deposition, Materials 13 (2020) 1721, https://doi.org/10.3390/ma13071721.

[10] Z. Cai, J. Wen, R. Wang, et al., Characteristics of tungsten coating on silicon particles prepared by sol-gel method, Mater. Chem. Phys. 305 (2023) 127942, https://doi.org/10.1016/j.matchemphys.2023.127942.

[11] H. Liu, S. Sabine, P. Marcin, et al., Preparation of superhydrophobic coatings on zinc, silicon, and steel by a solution-immersion technique, ACS Appl. Mater. Interfaces 1 (2009) 86–91, https://doi.org/10.1021/am900488w.

[12] T. Zhang, H. Chen, J. Sun, et al., Atomic simulation and experimental: oxidation protective SiC coating produced by chemical vapor deposition and pack cementation for carbon/carbon composites, Surface. Interfac. 46 (2024) 104170, https://doi.org/10.1016/j.surfin.2024.104170.

[13] S. Zhu, Y. Xu, X. Duan, et al., Enhancing high-temperature oxidation resistance of tantalum-tungsten alloy with composite coating, J. Alloys Compd. 1002 (2024) 175159, https://doi.org/10.1016/j.jallcom.2024.175159.

[14] Q. Yan, S. Chen, H. Shi, et al., Novel anti-oxidation coating prepared by polymer-derived ceramic for harsh environments up to 1200 °C, Surf. Coating. Technol. 494 (2024) 131420, https://doi.org/10.1016/j.surfcoat.2024.131420.

[15] C. Wang, W. Ping, Q. Bai, et al., A general method to synthesize and sinter bulk ceramics in seconds, Science (New York, N.Y.) 368 (2020) 521–526, https://doi.org/10.1126/science.aaz7681.

[16] S. Łukasz, B. Przemysław, G. Adam, Optimisation of mechanical properties of ZrC multilayer coatings, Thin Solid Films 704 (2020) 138016, https://doi.org/10.1016/j.tsf.2020.138016.

[17] B. Ma, J. Li, ZrB_2-SiC-ZrC coating on ZrC ceramics deposited by plasma spraying, Results Phys. 15 (2019) 102550, https://doi.org/10.1016/j.rinp.2019.102550.

[18] H. Ding, S. Jiang, J. Xu, Cavitation erosion resistance of ZrC nanoceramic coating, Proc. IME J. J. Eng. Tribol. 234 (2020) 833–841, https://doi.org/10.1177/1350650119873232.

[19] T. Liu, Y. Niu, C. Li, et al., Ablation resistance of ZrC-$MoSi_2$/ZrC-SiC double-layered coating in a plasma flame, Corrosion Sci. 145 (2018) 239–248, https://doi.org/10.1016/j.corsci.2018.10.006.

[20] D. Sun, Y. Cai, L. Zhu, et al., High-temperature wear behaviour of ZrC/NbC-reinforced CrMnFeCoNi coatings, Surf. Eng. 38 (2022) 778–785, https://doi.org/10.1080/02670844.2022.2153497.

[21] J. Huang, L. Guo, L. Zhong, Synergistic healing mechanism of self-healing ceramics coating, Ceram. Int. 48 (2022) 6520–6527, https://doi.org/10.1016/j.ceramint.2021.11.198.

[22] D. Kim, J. Lee, J. Choi, et al., Healing performance of a self-healing protective coating according to damage width, Coatings 10 (2020) 543, https://doi.org/10.1016/j.ceramint.2021.11.198.

[23] S. Hamed, S.A. Reza, K. Amir, et al., Self-healing coatings loaded by nano/microcapsules: a review, Protect. Met. Phys. Chem. Surface 58 (2022) 287–307, https://doi.org/10.1134/s2070205122020162.

[24] K. Takumi, M. Kent, S. Hiroki, et al., Improvement in the self-healing property of plasma-sprayed environmental barrier coatings by SiC addition, J. Therm. Spray Technol. 31 (2022) 2314–2326, https://doi.org/10.1007/s11666-022-01441-w.

[25] S. Fan, L. Zhang, L. Cheng, et al., Preparation and properties of self-healing coating for C/SiC brake materials, Int. J. Appl. Ceram. Technol. 5 (2008) 204–209, https://doi.org/10.1111/j.1744-7402.2008.02200.x.

[26] L. Zhou, W. Liu, Y. Mao, et al., A diffusion–reaction-deformation cohesiveinterface for oxidization and self-healing of PyC/SiC interfacial coating, Compos. Struct. 344 (2024) 118332, https://doi.org/10.1016/j.compstruct.2024.118332.

[27] H. Ouyang, C. Li, J. Huang, et al., Self-healing ZrB_2–SiO_2 oxidation resistance coating for SiC coated carbon/carbon composites, Corrosion Sci. 110 (2016) 265–272, https://doi.org/10.1016/j.corsci.2016.04.040.

[28] W. Liu, X. Ren, H. Chu, et al., Preparation of $MoSi_2$-SiB_6 oxidation inhibition coating on graphite by spark plasma sintering method, Surf. Coating. Technol. 405 (2020) 126511, https://doi.org/10.1016/j.surfcoat.2020.126511.

[29] Soontaranon S. Musyarofah, W. Limphirat, et al., XRD, WAXS, FTIR, and XANES studies of silica-zirconia systems, Ceram. Int. 45 (2019) 15660–15670, https://doi.org/10.1016/j.ceramint.2019.05.078.

[30] L. Kurpaska, Structural properties of zirconia–in-situ high temperature XRD characterization, J. Mol. Struct. 1163 (2018) 287–293, https://doi.org/10.1016/j.molstruc.2018.03.010.

[31] I.E. Muresan, D. Lutic, M. Dobrota, et al., Multimodal porous zirconium silicate macrospheres: synthesis, characterization and application as catalyst in the ring opening reaction of epichlorohydrin with acrylic acid, Appl. Catal. A Gen. 556 (2018) 29–40, https://doi.org/10.1016/j.apcata.2018.02.024.

[32] X. Zhu, L. Xu, C. Cui, et al., Preparation and characterization of zirconium carbide nano powder by hydrothermal and carbothermal reduction methods, Ceram. Int. 50 (2024) 30151–30160, https://doi.org/10.1016/j.ceramint.2024.05.314.

[33] M. E H, G. T N, Investigation of the nanocrystalline nature of silicon carbide (3C–SiC) nanoparticles by XRD and TEM methods, Mod. Phys. Lett. B 37 (2023) 2350072, https://doi.org/10.1142/s0217984923500720.

[34] G. Li, C. Cai, Y. Wang, et al., Zirconium silicate growth induced by the thermochemical interaction of yttria-stablized zirconia coatings with molten CMAS deposits, Corrosion Sci. 149 (2019) 249–256, https://doi.org/10.1016/j.corsci.2019.01.011.

[35] J. Kong, Y. Zhang, G. Chen, et al., Comparison of ablation performances and sublayer interaction of CVD-(TaC/SiC)3 alternate coatings with different crystallite morphologies, Surf. Coating. Technol. 483 (2024) 130801, https://doi.org/10.1016/j.surfcoat.2024.130801.

[36] F. De, W. Chuan, H. Cai, et al., XPS studies of surface oxidation of metal carbides, Fullerenes, Nanotub. Carbon Nanostruct. 30 (2022) 718–726, https://doi.org/10.1080/1536383x.2021.2014456.

[37] I.E. Muresan, D. Lutic, M. Dobrota, et al., Multimodal porous zirconium silicate macrospheres: synthesis, characterization and application as catalyst in the ring opening reaction of epichlorohydrin with acrylic acid, Appl. Catal. A Gen. 556 (2018) 29–40, https://doi.org/10.1016/j.apcata.2018.02.024.

[38] A. Ahmet, İ.Ç. Hakkı, Investigation of the density, porosity, and permeability properties of pervious concrete with different methods, Construct. Build. Mater. 294 (2021) 123539, https://doi.org/10.1016/j.conbuildmat.2021.123539.